ADVANCED FUNCTIONAL MATERIALS
www.afm-journal.de

Check for updates

A Fast Autonomous Healing Magnetic Elastomer for Instantly Recoverable, Modularly Programmable, and Thermorecyclable Soft Robots

*Yin Cheng, Kwok Hoe Chan, Xiao-Qiao Wang, Tianpeng Ding, Tongtao Li, Chen Zhang, Wanheng Lu, Yi Zhou, and Ghim Wei Ho**

Intrinsically self-healing stretchable polymers have been intensively explored for soft robotic applications due to their mechanical compliance and damage resilience. However, their prevalent use in real-world robotic applications is currently hindered by various limitations such as low mechanical strength, long healing time, and external energy input requirements. Here, a self-healing supramolecular magnetic elastomer (SHSME), featuring a hierarchical dynamic polymer network with abundant reversible bonds, is introduced. The SHSME exhibits high mechanical strength (Young's modulus of 1.2 MPa, similar to silicone rubber) and fast self-healing capability (300% stretch strain after 5 s autonomous repair at ambient temperature). A few SHSME-based robotic demonstrations, namely, rapid amphibious function recovery, modular-assembling-prototyping soft robots with complex geometries and diverse functionalities, as well as a dismembering–navigation–assembly strategy for robotic tasking in confined spaces are showcased. Notably, the SHSME framework supports circular material design, as it is thermoreformable for recycling, demonstrates autorepair for extended lifespan, and is modularizable for customized constructs and functions.

1. Introduction

Self-healing soft polymers, inspired by smart biological tissues, possess the unique combination of mechanical compliance and the capability to self-repair structural damages. These appealing merits make self-healing polymers extensively explored in various soft matter technologies.[1–5] Particularly, self-healing polymers are promising choices for soft robotics, which promises the integration of motion agility, human–machine interaction safety, and adaptability to unstructured environments.[6–10] These soft robotic devices have found their way into increasing industrial and biomedical scenarios.[11–16] In pursuit of further advancing the performance and bringing paradigm shift in design to soft robotics, it is essential to develop intrinsically self-healable and stretchable polymeric materials for the design and construction of soft robots. Current strategies rely on the incorporation of dynamic bonds into polymeric networks, including the dynamic covalent bonds, e.g., disulfide bonds,[17] dynamic urea bonds,[18] and Diels–Alder reaction;[19] and supramolecular noncovalent bonds, e.g., hydrogen bonds,[20,21,22] metal–ligand coordination,[23] host–guest interaction,[24] and hydrophobic interaction.[25] Vanderborght's group[26] developed a thermoreversible Diels–Alder polymer that healed the perforation damage under a controlled heating-and-cooling treatment. Yu's group[27] reported an anisotropic hydrogel capable of laser triggered incision repair through dynamic thiolate-metal coordination. More recently, Sitti and co-workers[28] introduced squid-inspired synthetic protein-based self-healing polymer that showed rapid healing through hydrogen bonding with assistive localized heating. Despite these progresses, the widespread use of self-healing polymers in real-world soft robotic applications are still hampered by their existing shortcomings of low mechanical strength (typically for hydrogels), long healing time (often requires several to tens of hours), functionality loss during repair, and the need for external input energy (heat, light, and/or continuous compression) to trigger efficient healing process.

With these concerns in mind, we hereby proposed a rational design of supramolecular polymeric network with the dispersion of magnetic microparticles within the elastic matrix through a simple and facile synthetic route. The synthesized self-healing supramolecular magnetic elastomer (SHSME) features a hierarchical network, composed of dynamic linear chains and crosslinkers, based on a biological molecule alpha lipoic acid (ALA). The high density dynamic motifs in the polymer network and the multiple dynamic interactions of covalent and noncovalent bonds endow the SHSME material not only high mechanical strength (Young's modulus of 1.2 MPa, ultimate tensile stress of 0.4 MPa), but also a fast autonomous self-healing ability. Upon destructive cut-through damage, the SHSME was able to sustain a stretch strain of 300% after 5 s

Y. Cheng, K. H. Chan, X. Wang, T. Ding, T. Li, C. Zhang, W. Lu, Y. Zhou, Prof. G. W. Ho
Department of Electrical and Computer Engineering
National University of Singapore
4 Engineering Drive 3, Singapore 117583, Singapore
E-mail: elehgw@nus.edu.sg

The ORCID identification number(s) for the author(s) of this article can be found under https://doi.org/10.1002/adfm.202101825.

DOI: 10.1002/adfm.202101825

 © 2021 Wiley-VCH GmbH

self-healing duration at ambient temperature (20 °C) without any external intervention. The SHSME material achieved a good balance in resolving the trade-off between the desired mechanical strength and rapid self-healing performance.

To illustrate the attributes of SHSME for soft robotics, we devise a robotic material circular design by incorporating three conceptual principles of i) thermoreformable material for product adaptation to users' changing needs, ii) autorepair for extended lifespan of products, and iii) modularizable scheme for continuous variable of customized constructs and functions. We first demonstrate a magnetic water-spider soft robot thermally molded from the SHSME material. The water-spider with multiple locomotion ability exhibited nearly instantaneous robotic function recovery from lacerated damages both on the ground and underwater. By virtue of the fast self-healing of the thermoreversible SHSME, we further propose a closed-loop rapid prototyping platform via free modular assembly and integration, for multifunctional 3D architectured soft robots, with an artificial robotic tendril, a multiterrain carrier, and a multimodal electronic switch (E-switch). Last, a dismembering–navigation–assembly strategy is presented to allow the remote contactless magnetic assembly for implementing tasks within confined spaces. The SHSME material addresses limitations in self-healing performance, opens up versatile design space for multifunctional soft robots, and inspires paradigm shift in robotic tasking within confined space.

2. Results and Discussion

2.1. The Synthesis and Self-Healing Mechanism of the SHSME Material

In order to build a hierarchical polymer network with abundant dynamic bonds, naturally existing biological molecule ALA was chosen as the starting material, as this biocompatible monomer exhibits a small and tailored molecular structure with disulfide bond in a five-membered ring and pendent carboxylic group. Thermal-initiated ring-opening polymerization of ALA results in primary linear backbone chains, and subsequent cooling allows the hydrogen bonding formation through dimerization of carboxylic groups in between the linear chains to form a transparent and soft polymer. However, disulfide bonds in ring structures suffer from inverse ring-opening depolymerization due to terminal diradicals, which makes the metastable polymer turn opaque and rigid (Figure S1, Supporting Information). Previous studies have tried to utilize divinyl monomers to copolymerize such polymer melt for stabilization, yet it introduces permanent covalent network into the resultant polymer that undermines the overall dynamic feature.[29–33]

To address this issue, here, we introduce ferric ions (Fe^{3+}) alone into the polymer melt to work as strong complex centers with carboxylic groups, which crosslink the dynamic backbone chains, instead of using divinyl monomers to form covalent crosslinks in the polymer matrix. When the mass ratio of ferric chloride ($FeCl_3$) to ALA exceeds 0.02%, we found the obtained transparent and soft polymer poly(ALA-Fe) maintained thermodynamically stable (Figure S2, Supporting Information). Hard magnetic microparticle, neodymium-iron-boron (NdFeB), which features high remnant magnetization and coercivity, was added into the host gel to form a uniform dispersion (see Figure S3 in the Supporting Information for scanning electron microscopy (SEM) characterization and elemental mapping). **Figure 1**a depicts the schematic of the hierarchical dynamic SHSME network. Multiple characterization techniques were used to confirm the structure of SHSME. X-ray diffraction (XRD) of poly(ALA-Fe) exhibited no crystalline peaks, indicating the amorphous state and no formation of iron oxide in the polymer matrix (Figure S4, Supporting Information). Raman spectra in Figure S5 in the Supporting Information shows a splitting of peak at 507 cm^{-1} (attributed to disulfide bonds of ALA) into two pronounced peaks at 503 and 521 cm^{-1} for poly(ALA-Fe), verifying the successful ring-opening polymerization of ALA. In Fourier transform infrared (FTIR) test (Figure S6, Supporting Information), the coordination bonds between carboxylic group and Fe^{3+} was substantiated by shifting of the peak from 1686 to 1700 cm^{-1}. The optimized $FeCl_3$ to ALA mass ratio was 0.06% to achieve a long-term stable, mechanically strong, and resilient SHSME (Figures S7 and S8, Supporting Information). The SHSME was magnetized to saturation by a uniform magnetic field of 2T, with a mass ratio of magnetic microparticle to ALA monomer of 0.5 (Figure S9, Supporting Information). Unless otherwise specified, such optimized formulation was kept for subsequent tests and utilization.

The small molecular structure of ALA and multiple reversible bonding types (covalent disulfide bond, noncovalent hydrogen bond, and metal–ligand coordination bond) collectively contribute to a high density of reversible associations within a hierarchical dynamic polymer network. When the SHSME is damaged or ruptured, breakage of these reversible bonds occurs at the interface, resulting in high concentration of dissociated groups and dangling chains near the newly generated surfaces. With such high density of dissociated moieties, combined with the relatively long dangling chains (four-carbon-alkyl chains) to which the carboxyl groups are attached, we speculate it can facilitate a fast self-healing process that is dominated by an efficient recombination regime through the anomalous diffusion (diffusive Rouse motion of dangling chains leads to encountering of dissociated groups; Figure S10, Supporting Information).[34–36] Figure 1b shows the schematic of the abnormal homopolar bonding of two magnetized SHSME pieces enabled by the fast interface bonding, indicating the capability to readily program the localized magnetization profiles in SHSME-based structures. To illustrate its efficacy in magnetically controlled soft actuation, an SHSME stick was constructed by homopolar bonding of three short magnetized SHSME units ($1.5 \times 1.5 \times 14$ mm). The firmly bonded stick (characterization of the homopolar repulsive force and the mechanical tensile test of the stick in Figure S11 in the Supporting Information) underwent fast, reversible, and predictable shape transformation from "I" to "S" upon applied uniform magnetic field B, as shown in Figure 1c.

The SHSME possesses high thermal stability in a wide temperature range as the thermogravimetric analysis (TGA; Figure S12, Supporting Information) revealed an initial decomposition temperature of around 200 °C. The glass transition temperature (T_g) was measured to be –19.2 °C from the differential scanning calorimetry (DSC; Figure S13, Supporting

© 2021 Wiley-VCH GmbH

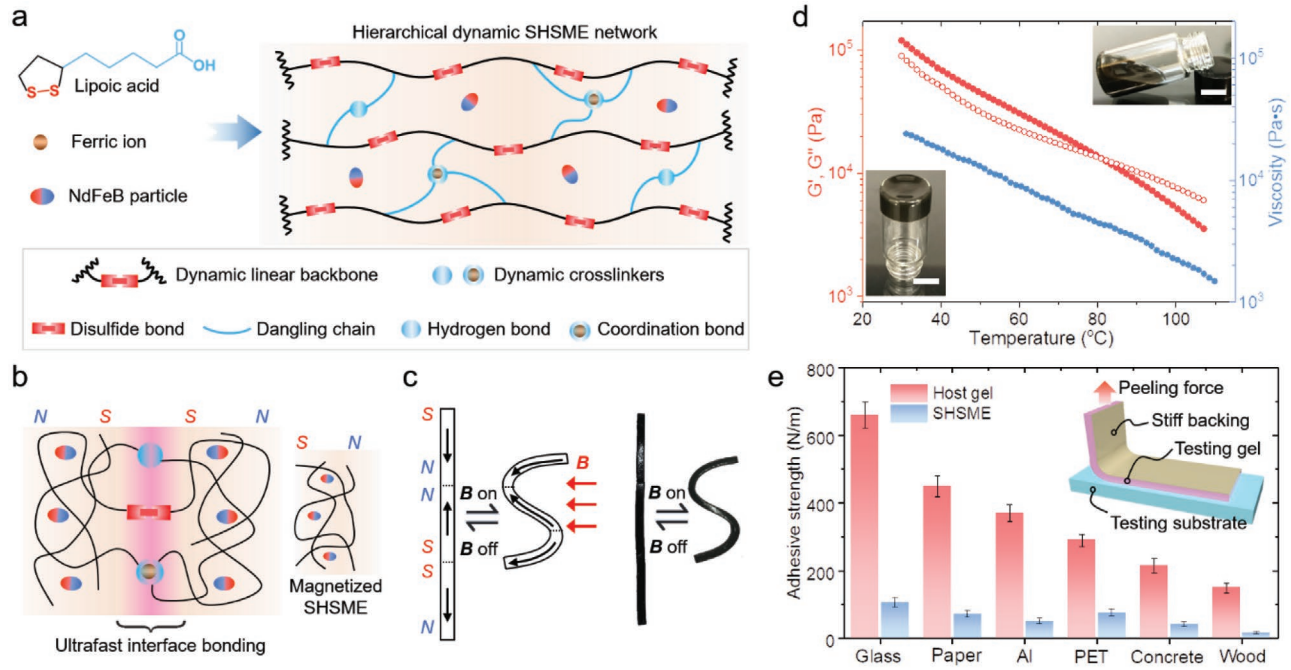


Figure 1. The synthesis, self-healing mechanism, and characterization of the SHSME material. a) Schematic of the proposed hierarchical dynamic polymer network of SHSME. b) Schematic description of the fast interface bonding through multiple dynamic interactions and the homopolar bonding. c) Schematic illustration (left) and experimental result (right) of shape transformation of an SHSME-based stick under uniform magnetic field *B* (150 mT). The magnetization profile was forced to align with applied magnetic flux. d) Temperature dependency of storage (red solid dots, *G′*) and loss (red hollow dots, *G″*) moduli and viscosity (blue dots) of SHSME. The inset lower and upper photos show the SHSME at cooled (20 °C) and heated (90 °C) states, respectively. Scale bars, 10 mm. e) 90° peeling tests of the host gel and SHSME toward various substrates. The inset illustrates the 90° peeling test.

Information). The low T_g suggested the favorable high chain mobility at room temperature for autonomous self-healing. Figure 1d shows temperature sweeping rheological tests to SHSME: The storage modulus *G′* and loss modulus *G″* both decreased with an increase in temperature, and *G″* surpassed *G′* at a temperature higher than around 80 °C, indicating a solid-like to liquid-like transition of viscoelastic behavior. Moreover, the melt viscosity declined persistently with an increase of temperature, due to the heat-labile hydrogen bonds, disulfide bonds, and enhanced chain mobility. The strong temperature dependence of viscosities makes the SHSME material easily processable (can be molded or extruded), reusable, and recyclable. Also worth noting is the tremendous change in adhesive properties for the poly(ALA-Fe) host gel and SHSME. From 90° peeling test results in Figure 1e (see Figure S14 in the Supporting Information for detailed testing curves), the host gel revealed strong adhesive strength to various substrates ranging from 150 to 660 N m^{-1}, including glass, paper, aluminum (Al), polyethylene terephthalate (PET), concrete, and wood. Once coming into contact, the host gel affixed itself firmly to these substrates owing to the rich carboxylic groups in its matrix to form hydrogen bonds with other surfaces (Figure S15, Supporting Information). After dispersion of NdFeB microparticles, the SHSME went through drastic decrease in adhesion, ranging from 15 to 105 N m^{-1}. Consequently, the SHSME lost the firm adhesion to other substrates, which affords SHSME-based soft robots to freely locomote or interact with surrounding environments. From the optical microscope analysis (Figure S16, Supporting Information), we speculated that the NdFeB microparticles on the surface of SHSME reduced the areal presence of the sticky poly(ALA-Fe) and increased the surface roughness, both of which collectively contributed to the overall nonadhesiveness.

2.2. Ultrafast Self-Healing Properties

To verify the fast autonomous self-healing capability of the SHSME material, tensile stress–strain tests (**Figure 2**a) were conducted on the original sample and the healed samples in ambient environment (20 °C in air). The original SHSME showed a high stretchability of 675% strain, Young's modulus of 1.2 MPa (calculated from low strain region of <10% strain), and ultimate tensile stress of 0.4 MPa at a stretching speed of 80 mm min^{-1} (constant for tensile tests). The healed samples were cut through into two pieces and subsequently put together to allow healing for varying durations. As expected, a longer healing time led to a higher recovered elongation strain (Figure S17, Supporting Information), considering the improved probability of the dynamic dissociated groups to encounter and recombine with each other via anomalous diffusion. A self-healing duration of 5 min caused a maximum elongation strain of 615%, corresponding to a high self-healing efficiency (η) of 91% in terms of the recovered fracture strain. A prolonged healing time to 10 min resulted in almost fully recovered mechanical properties (η of 99%). Note that the introduction of the magnetic microparticles slightly decreased the self-healing

© 2021 Wiley-VCH GmbH

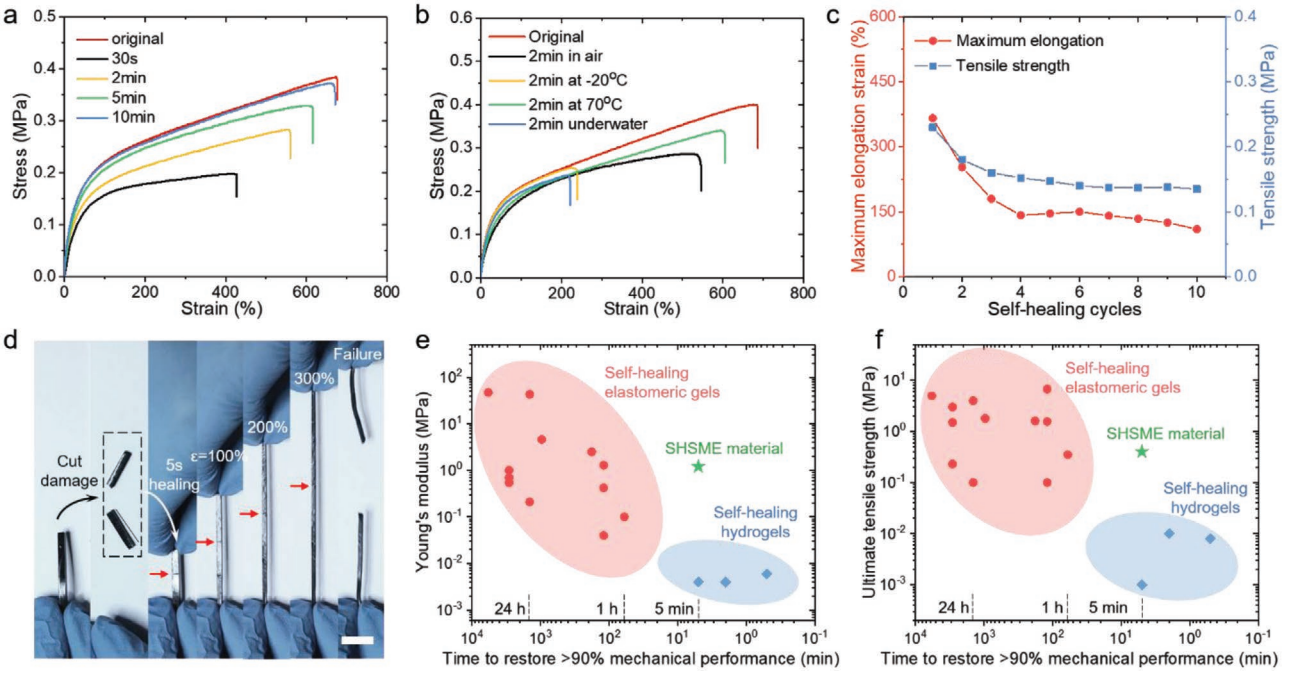


Figure 2. Fast autonomous self-healing properties of the SHSME material. a) The tensile stress–strain curves of the original and self-healed SHSME with varying healing durations. b) The tensile stress–strain curves of the original and self-healed SHSME under different healing conditions. c) Cyclic self-healing tests of the SHSME for ten cycles by repeatedly stretching the sample to fracture and healing for 30 s in each cycle. d) Digital images of cutting an SHSME stick (2 × 2 × 25 mm) into two pieces, self-healing for 5 s, and then stretching the healed sample till failure. Scale bar, 10 mm. e,f) Comparison of our SHSME material with other synthetic self-healing polymers in terms of the Young's modulus and time duration to autonomously restore >90% maximum elongation strain.

efficiency compared with the host polymer matrix, possibly due to the appearance of the microparticles at the cutting interface and resultant decrease of the contact area of the polymer matrix (Figure S18, Supporting Information). Besides ambient environment, the SHSME was also self-healable under extreme conditions. Figure 2b shows the 2 min duration self-healing testing results under high (70 °C) and ultralow (−20 °C) temperatures in air and underwater (20 °C). Compared with the 2 min duration self-healing efficiency in ambient environment (η of 80%), the self-healing efficiencies at 70 and −20 °C were 89% and 35%, respectively (Figure S19, Supporting Information). The promoted healing performance under high temperature was probably attributed to the combination of the enhanced chain mobility and dynamics of the reversible bonds. Healing underwater (the whole process of cutting and healing was kept underwater) for 2 min exhibited a self-healing efficiency of 32%, and the degraded healing performance could be caused by the absorption of moisture onto the freshly cut interfaces to form hydrogen bonding with carboxylic groups. Fast and repeatable self-repair is crucial for reliable and resilient real-world applications. We here tested the multicycle self-healing ability of the SHSME by repeatedly stretching the sample to fracture and self-heal for 30 s in each cycle (Figure S20, Supporting Information). Figure 2c indicates that the maximum elongation strain and tensile strength both decreased in the first four cycles and then leveled off at a strain of 150% and tensile fracture strength of 0.14 MPa, suggesting reliable multicycle self-healing ability under harsh testing conditions (continuous damage and short recovery time).

To better demonstrate the fast autonomous self-healing ability, an SHSME-based stick sample was cut and immediately healed for 5 s and then stretched till failure, as seen in Figure 2d (Video S1, Supporting Information). The SHSME material was able to sustain a stretch strain as large as 300% after only 5 s self-healing at room temperature (20 °C) from destructive cut-through damage. We also summarized the Young's modulus (mechanical stiffness) and ultimate tensile stress (mechanical strength) versus the time length ($t_{90\%}$) required to autonomously recover >90% maximum elongation strain of recently reported self-healing polymers in Figure 2e,f, respectively (details in Table S1 in the Supporting Information). Self-healing polymers in the form of hydrogels exhibit impressively rapid healing speed,[37–39] with $t_{90\%}$ ranging from half a minute to five minutes, as the solvent surrounding the polymer network acts as lubricant and enormously boosts the chain mobility and dynamics of the reversible chemical bonds. However, these hydrogels tend to have low Young's modulus and mechanical strength (typically both below 100 kPa), which are desired for biomedical tissue engineering, but disadvantageous for soft robotic applications where mechanical self-supporting and load-bearing features are required. Self-healing polymers in the form of dry gels are primarily supramolecular elastomers that integrate dynamic functional moieties into existing elastic macromolecular polymer networks.[40–51] These elastomeric gels show a wide tunable range of mechanical strength (Young's modulus from tens of kPa to tens of MPa, ultimate tensile stress from tens of kPa to several MPa) derived from the specific combination of macromolecular species and the dynamic chemistry

© 2021 Wiley-VCH GmbH

types. However, they often need a prolonged time scale to reach a 90% healing efficiency, with $t_{90\%}$ ranging from several to tens of hours. In contrast, our SHSME material managed to achieve a good balance with a decent mechanical strength (Young's modulus of 1.2 MPa and ultimate tensile stress of 0.4 MPa) and fast autonomous self-healing ability (5 min to accomplish a 90% self-healing efficiency) simultaneously. This exceptional accomplishment stems from the elaborate hierarchical dynamic network with high density of dynamic chemical bonds.

2.3. SHSME Based Water-Spider Soft Robot with Amphibious Self-Healing Ability

The fast autonomous self-healing ability of SHSME holds great promises for reliable and robust soft robotic performance, which is sought-after for tasks in unpredicted and unstructured environments. As the thermally tunable viscosity allows easy processing through molding, we cast the SHSME melt (90 °C) into a polydimethylsiloxane (PDMS) mold and cooled it down to obtain a magnetic water-spider soft robot, as illustrated in **Figure 3**a. The water-spider soft robot was further magnetized to obtain a single-wavelength harmonic magnetization profile along the body length (Figure S21, Supporting Information). In this work, we utilized permanent magnets to remotely apply variable magnetic field through translational and rotational movements (Figure S22, Supporting Information). The magnetic field-induced torque and magnetic gradient-induced pulling force were harnessed to drive the shape change and motions of the magnetic soft robots. As shown in Figure 3b, the presence of magnetic field in the *x*-axis direction caused the deformed (bend to align magnetic profile with the applied magnetic flux) water-spider robot to stand up (Figure S23, Supporting Information). The rotation of the magnetic field about the *z*-axis and *y*-axis enabled the water-spider robot to adjust orientations (Figure S24, Supporting Information) and roll forward (Figure S25, Supporting Information), respectively. The multiple locomotion types are demonstrated in Video S2 in the Supporting Information. The roll-forward locomotion was further employed to accomplish cargo transport task (approach, pick up, transport, and release) by adjusting the magnitude of magnetic field to tune the bending curvature of the water-spider soft robot (Figure 3c; Figure S26 and Video S3, Supporting Information). Besides these on-ground locomotion types, the hydrophobic surface of the SHSME material (Figure S27, Supporting Information) also allows the surface tension of water to support the water-spider robot (measured density of 1.55 g cm^{-3}) on water. Figure 3d shows the magnetic gradient-based directional steering of the water-spider robot to float in the desired route. Note that the dimensions of the SHSME-based soft robots could be further scaled down to submillimeter through the mold-casting strategy, and a rectangular shaped SHSME-based robot (0.28 × 0.4 × 2 mm) is demonstrated in Figure S28 in the Supporting Information.

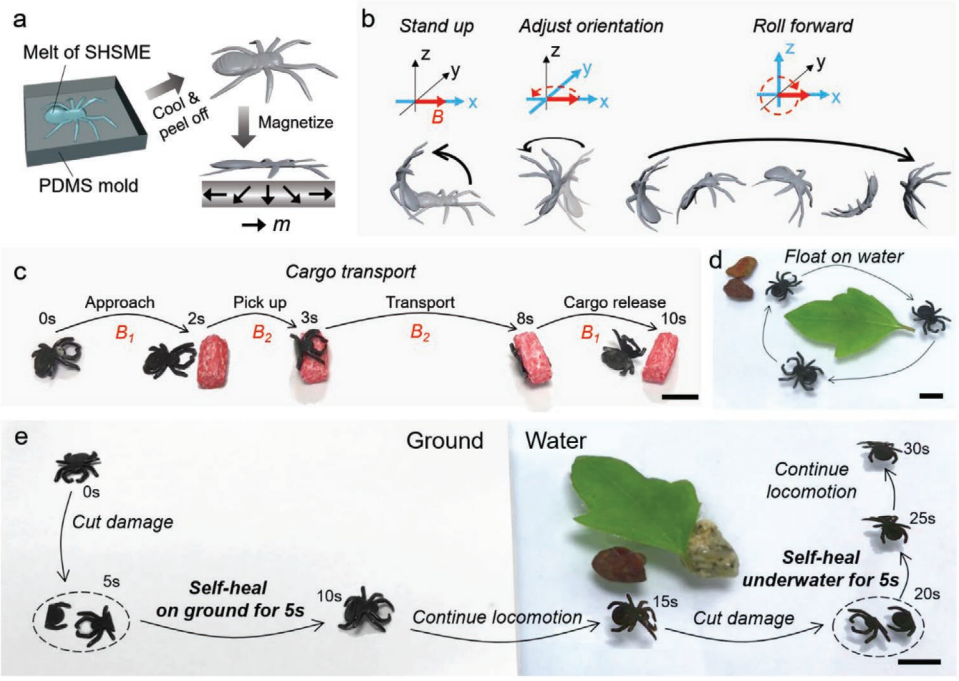


Figure 3. SHSME-based water-spider soft robot with amphibious self-healing ability. a) Schematic shows the fabrication and magnetization profile of the SHSME water-spider. The robot size is 10 × 6 × 1 mm. b) Schematic shows the three types of locomotion (stand up, adjust orientation, and roll forward) and the corresponding triggering magnetic field (magnitude of around 10 mT). c) Digital image shows the cargo (a red foam, 8.5 mg) transport tasking. The relatively small magnitude of B_1 (≈10 mT) led to small bending curvature for approaching the cargo, and larger magnitude of B_2 (≈40 mT) led to increased bending curvature for pick-up and transport. Magnetic field was withdrawn to release the cargo. d) Digital image shows the water-spider soft robot floats on water. The magnitude of magnetic field to drive the robot was around 2 mT. e) Digital image shows the water-spider soft robot rapidly recovered its locomotion from cut-through damage upon 5 s self-healing, and resumed the expedition both on the ground and underwater. All scale bars, 10 mm.

© 2021 Wiley-VCH GmbH

As the combination of the designed structure and magnetization profile together contributes to robotic motions of soft robots, mechanical damages (such as the destructive cutting damage) certainly disrupt the structural and magnetic pattern integrity of the designed robots, which inevitably affects or even disables robotic functionalities. In our case, the water-spider failed to perform the cargo pick-up and transportation after being cut into two pieces. To verify the amphibious self-healing ability of the SHSME-based water-spider soft robot, we maneuvered the robot from ground to underwater, as seen in Figure 3e. We inflicted catastrophic cut damages to the water-spider robot during both on-the-ground and underwater expeditions. We found that upon rapid 5 s self-healing from each damage, the water-spider soft robot emerged unscathed, incredibly restored sufficient structural strength to recover the locomotion ability, and resumed its operation (Video S4, Supporting Information). Such almost instantaneous recovery of robotic performance both on ground and underwater suggested that the SHSME material is particularly suitable for robotic applications in uncontrolled environments to survive and endure unanticipated damages.

2.4. SHSME Based Closed-Loop Modular Assembly for Functional Soft Robots

Soft robots targeting at diverse functional scenarios inevitably bring about demands for well-designed sophisticated 3D robot structures. Inspired by the fast autonomous self-healing of SHSME, we developed a closed-loop free modular assembly platform for rapidly prototyping magnetic functional soft robots with complex 3D geometries. **Figure 4**a illustrates the workflow: first, a bulk SHSME sheet was transformed into 1D/2D/3D building blocks using simple and direct customized tailoring, including cutting, flexing, and heat-setting (Figure S29, Supporting Information). Second, we obtained magnetic modules by selectively magnetizing these building blocks with prescribed magnetization profiles, and assembled them into designed architectures through fast self-healing. The piecing of the modules into an integrated robust structure typically requires several minutes. In this way, magnetic soft robots not only can be constructed into intricate 3D structures through modular assembly, but also encoded with locally

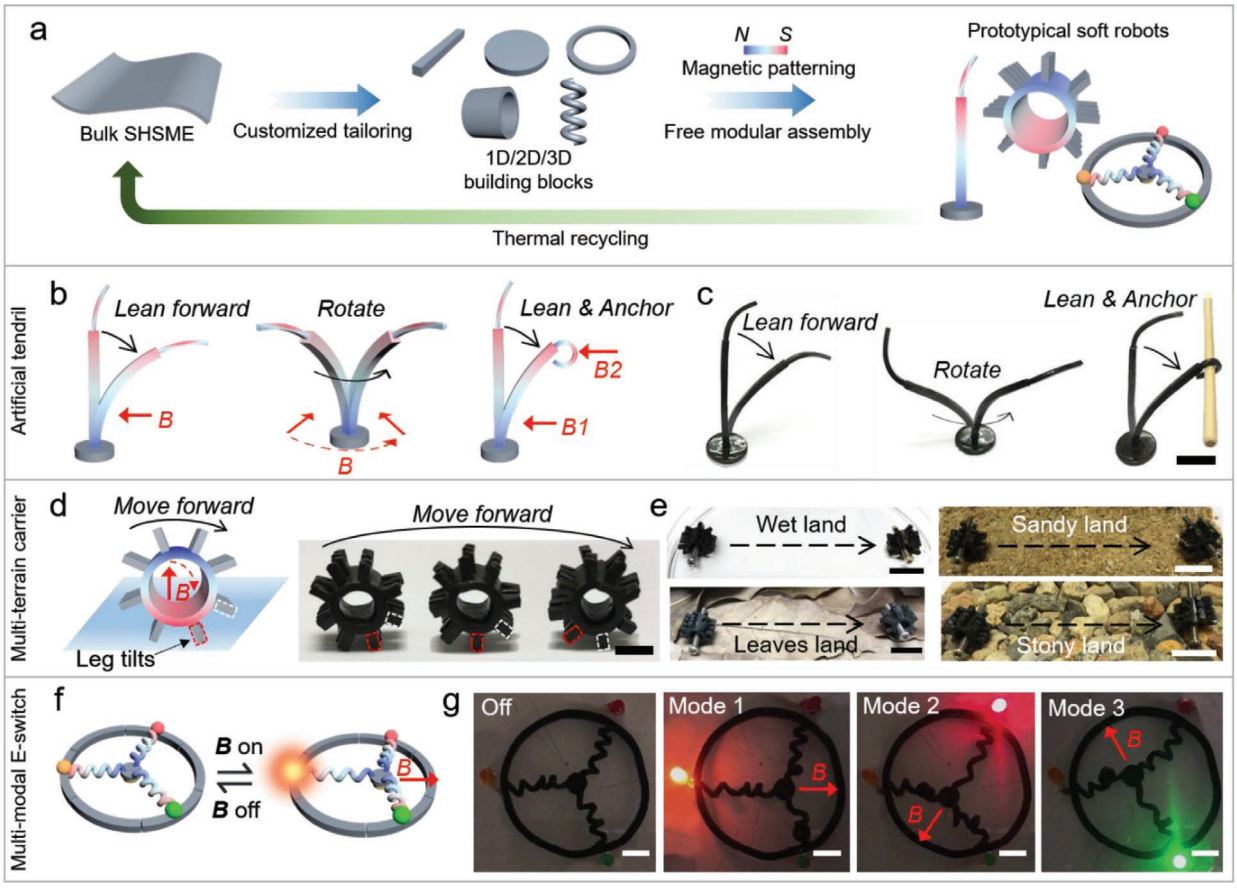


Figure 4. SHSME-based closed-loop free modular assembly. a) Schematic of the closed-loop modular assembly platform to design soft robots with diverse functionalities. The magnetic polarity of the magnetized building blocks is illustrated by blue (magnetic north) or red (magnetic south) color. b) Schematic of the magnetically controlled robotic motions of the artificial tendril. The magnitude of B, B_1, and B_2 was around 30 mT. c) Digital images show the robotic motions of the artificial robotic tendril. Scale bar, 20 mm. d) Schematic (left) of the structure design and locomotion mechanism of the multiterrain carrier, and digital images (right) of the forward moving locomotion. The magnitude of B was around 50 mT. Scale bar, 10 mm. e) The multiterrain carrier transports a cargo (a metal screw) and traverses various terrains. Scale bars, 20 mm. f) Schematic of the design and working principle of the multimodal E-switch. g) Digital images show the different modes of the E-switch under different magnetic fields. The magnitude of B was around 100 mT. Scale bar, 10 mm.

© 2021 Wiley-VCH GmbH

programmable magnetic patterns. Such modularly programmable structures and magnetic patterns cooperatively impart wide design space for various robotic functionalities, with three prototypical magnetic soft robots (an artificial robotic tendril, a multiterrain carrier, and a multimodal E-switch) as proof-of-concept examples (Figure S30 in the Supporting Information for detailed dimensions and magnetization patterns). Third, the dynamic nature of the polymer network endows the SHSME-based soft robots with recyclability. The SHSME-based structures were cut into pieces and heated to melt to allow reshaping for multiple reusing, with no significant mechanical property degradation (Figure S31, Supporting Information). This thermal recyclability makes the fast prototyping platform a closed-loop system in materials utilization, which is essential for an eco-friendly and sustainable robotic industry.

We then introduced the robotic functionalities of the prototypical soft robots enabled by the free modular assembly platform. Climbing plant tendrils are frequently mimicked because of their intriguing locomotion and anchoring mechanisms.[52,53] Figure 4b illustrates that the artificial tendril freely adapts its shape to the applied magnetic field B. When B accessed the bottom part and rotated, it drove the tendril to lean forward and rotate accordingly. The magnetic fields B_1 and B_2 sequentially approached the bottom and top parts, which then prompted the artificial tendril to lean toward and anchor to the target. Figure 4c shows the corresponding robotic motions of the artificial tendril (Video S5, Supporting Information), confirming the successful biomimetic functions, aka climbing plant tendrils.

Untethered soft robots with terrain crossing and cargo carrying functions are highly desirable for field operations in unstructured environments. As seen in Figure 4d, a multiterrain carrier with toothed-gear-like architecture was constructed by assembling stick-shaped legs onto a tube-shaped roller. The rotation of the applied magnetic field B exerted a clockwise torque on the magnetized roller, which forced the standing legs to tilt until the adjacent legs came into contact with ground, leading to forward moving locomotion of the robot. Figure 4e shows that the multiterrain carrier robot is not only capable of moving on dry and flat land, but also able to transport a cargo and traverse various difficult terrains, including wet land, leaves land, and sandy and stony lands (Video S6, Supporting Information).

The fast shape transformation of SHSME can potentially serve as functionally reconfigurable soft electronics by combining the soft robotic structures with electronic components and circuitry. Figure 4f illustrates the design and working principle of a multimodal E-switch. The magnetized spring component deflected to align with the magnetic field B, and elongated under the magnetic gradient-induced pulling. In this way, the applied magnetic field steered the copper ring in the center to move in the desired direction to the fixed switch contacts and closed the corresponding circuit. Figure 4g shows the "off" state when no magnetic field was applied, and three different electronic modes that turned on orange, red, and green light emitting diodes (LEDs), respectively, with specific magnetic field direction (Video S7, Supporting Information).

2.5. SHSME Based Dismembering-Navigation-Assembly Strategy for Robotic Tasking in Confined Space

Robotic operations within confined spaces (typically enclosed area with limited means of access) are widely needed in industrial applications for inspection, repairing, or maintenance. Soft robots can substantially improve the operation dexterity and obviate possible on-site exposure to hazards for tasks in confined spaces. However, the restricted access to such confined spaces poses a formidable challenge to the deployment of soft robots, especially when the dimensions of the desired robots considerably surpass that of the access passage.

To address this issue, we propose an SHSME-based dismembering–navigation–assembly strategy to bypass the dimension limitations. Essentially, a bulk magnetized SHSME material was able to be dismembered into elementary segments to allow easy navigation into confined spaces, and remotely assembled into desired 3D architectures via noncontact magnetic assembly, as illustrated in **Figure 5**a–c. To better demonstrate the efficacy of this strategy, we set up a task scenario as shown in Figure 5d. We have staged a narrow entrance channel to an enclosed space, in which there is a ditch that prevents the SHSME-based water-spider soft robot from transporting the cargo to the destination across the ditch. The navigation routings through the constrained environment are as described. The bulk SHSME sheet was first magnetized and cut into stick-shaped elementary segments (Figure 5a), and then the slim segments crawled through the "S" shaped tube channel into the enclosed space using a magnetically controlled creep-forward locomotion (Figure 5b,e; Video S8, Supporting Information). In view of the magnetic assembly and fast autonomous self-healing properties of SHSME, the elementary segments were assembled and welded into a multilegged robot through head-to-tail, shoulder-by-shoulder, and leg grafting assembling configurations (Figure 5c; Figure S32 and Video S9, Supporting Information). Finally, the multilegged robot maneuvered into the ditch and served as a bridge for the water-spider soft robot to transport the cargo to the opposite destination (Figure 5f; Video S10, Supporting Information).

3. Conclusion

Soft robots are generally tolerant of blunt damages (like impact, bending, and compression), however, they are extremely vulnerable to destructive/lacerative mechanical damages (puncture and cut) due to their inherent softness. The structural damage can degrade the performance or even disable the robotic function. In an effort to develop high-performance self-healing and stretchable polymer for the design of soft robots, we propose a facile synthetic method for supramolecular magnetic polymer SHSME, which features a combination of dynamic linear backbones and crosslinkers. The small molecular structure and the multiple reversible bonds derived from the monomer ALA afford a high density of dynamic bonds in the polymer network, which gives rise to a fast autonomous self-healing. The SHSME material can sustain a stretch of 300% after merely 5 s self-healing from destructive cut-through damage, which made it especially well-suited for soft robotic applications where instant functionality recovery from unpredicted damages is needed. We

© 2021 Wiley-VCH GmbH

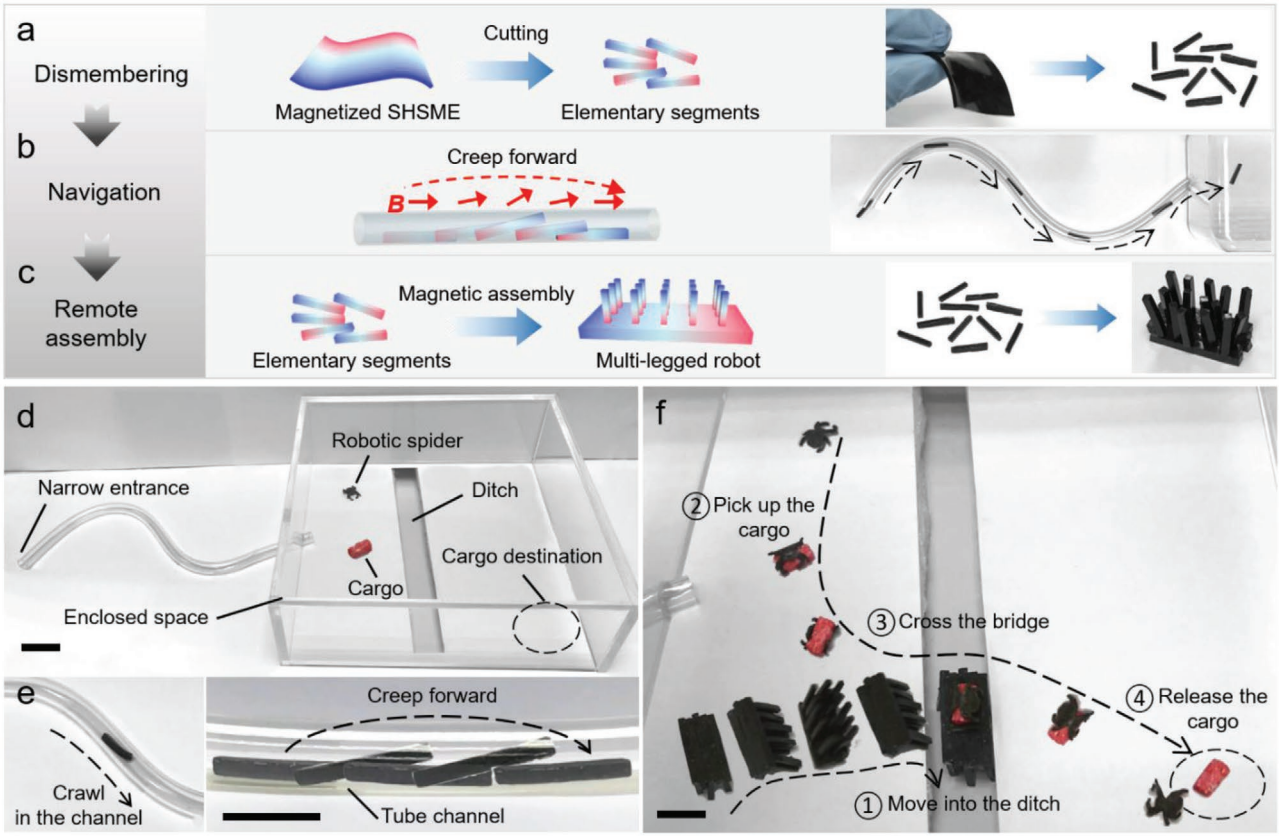


Figure 5. SHSME-based dismembering–navigation–assembly strategy. a) Schematic (left) and digital image (right) show the dismembering of a bulk SHSME sheet into elementary segments ($2 \times 2 \times 15$ mm). b) Schematic of the navigation of the SHSME segments in a narrow tube channel (diameter of 6 mm). The direction of *B* (10 mT) flapped up and down periodically to overcome frictional resistance of the segment with the tube, and the magnet moved along the "S" shaped passage simultaneously to drag the segment forward via the magnetic gradient-induced pulling force. Optical image shows the crawling along the "S" shaped tube channel. c) Schematic of the remote magnetic assembly of SHSME segments into a multilegged robot. Digital image shows the assembled multilegged robot. The leg size was $2 \times 2 \times 15$ mm, and the body part was $30 \times 10 \times 2$ mm assembled from 10 segments. d) A typical task scenario that involves confined space with restricted access. Scale bar, 20 mm. e) Digital image shows the SHSME segment crawled through the tube channel. Scale bar, 10 mm. f) Digital image shows the task accomplishment process. Scale bar, 10 mm.

demonstrated the SHSME-based water-spider soft robot with multimodal locomotion and amphibious self-healing ability. More importantly, an SHSME-based closed-loop free modular assembly was developed to make the fast and easy prototyping of complex 3D structured soft robots with diverse robotic functions accessible. Last, to address the challenging issue of robotic tasks in confined space, an SHSME-based dismembering–navigation–assembly strategy was put forward to enable the navigation and integration of soft robots within enclosed space. The concept of the hierarchical dynamic network can inspire the design of fast self-healing supramolecular polymers, and the superior self-healing performance can be extended from soft robotics to other application fields such as soft electronics and bioengineering.

4. Experimental Section

Synthesis of the SHSME Material: 5 g of ALA (Adamas, 13428D) was heated in oil bath to 140 °C to get a liquid-like melt. Controlled amount (mass ratio to ALA varying from 0.02% to 0.4%) of $FeCl_3$ (Sigma-Aldrich, 157740) was added into the ALA melt and magnetically stirred for 5 min to get the transparent and soft polymer poly(ALA-Fe) as the host gel. To obtain the SHSME material, the poly(ALA-Fe) melt was cooled to 90 °C, and then NdFeB microparticles (Magnequench, MQFP-B-20052-089) of varying mass ratio (from 0.1 to 0.5) was added into the host gel melt under stirring for 20 min to ensure homogeneous dispersion. The melt mix can be cooled to room temperature to obtain the SHSME material.

Material Characterization, Rheological Test, and 90° Adhesive Test: The SEM characterization was accomplished using a JEOL JSM-7001F field emission scanning electron microscope. The XRD test was conducted using diffractometer (GADDS XRD system, Bruker AXS). The Raman testing was performed with a DXR Raman Microscope (Thermal Scientific Corporation, USA, with a 780 nm excitation length). The FTIR testing was performed using an IR Prestige-21 by Shimadzu. The TGA test was conducted from 30 to 450 °C at a temperature rate of 10 °C min^{-1} using DTG-60H (Shimadzu). The DSC test was conducted from −50 to 120 °C at a temperature rate of 10 °C min^{-1} using a differential scanning calorimeter (DSC Q200, TA Instruments). The temperature-related rheological tests were performed using a MCR302 rheometer (Anton Paar). Viscometry measurements were carried out over a shear rate of 0.5 s^{-1} from 110 to 30 °C. Oscillatory sweeps were performed at 1 Hz within shear strain of 5% from 110 to 30 °C. The 90° peeling test between the host gel/SHSME and various other substrates (glass, paper, Al, PET, concrete, and wood) was conducted using a 90° peeling fixture (Texture Analyzer, CT3). Sample size was 60 × 10 × 1.5 mm. A 70 µm thick Kapton film was glued to the tested gel to work as stiff back

© 2021 Wiley-VCH GmbH

for prevention of excessive tensile stretching. At a stretching speed of 30 mm min^{-1}, the measured peeling forces per width of the tested gel was recorded and the interfacial adhesive strength was determined by dividing the plateau force by the width of the tested gel.

Self-Healing Efficiency Test: To test the self-healing efficiency, samples (2.5 × 2.5 × 16 mm) of the SHSME material were cut into two pieces at the middle position and subsequently put back together to allow self-healing under different conditions. For the underwater self-healing test, the whole process of cutting, putting back, and self-healing was conducted underwater. After specific self-healing duration under different conditions, tensile stress–strain tests were implemented to the healed samples at a stretching speed of 80 mm min^{-1} using a universe testing machine (MultiTest-i, Mecmesin).

Supporting Information

Supporting Information is available from the Wiley Online Library or from the author.

Acknowledgements

This research was supported by A*STAR under its 2019 AME IRG & YIRG Grant Calls, A2083c0059.

Conflict of Interest

The authors declare no conflict of interest.

Data Availability Statement

Research data are not shared.

Keywords

amphibious self-healing, magnetic soft robots, modular assembly, supramolecular elastomers

Received: March 17, 2021
Revised: May 4, 2021
Published online: June 4, 2021

[1] K. Parida, G. Thangavel, G. Cai, X. Zhou, S. Park, J. Xiong, P. S. Lee, *Nat. Commun.* **2019**, *10*, 2158.
[2] Y. J. Tan, H. Godaba, G. Chen, S. T. M. Tan, G. Wan, G. Li, P. M. Lee, Y. Cai, S. Li, R. F. Shepherd, J. S. Ho, B. C. K. Tee, *Nat. Mater.* **2020**, *19*, 182.
[3] Y. Wu, L. Wang, X. Zhao, S. Hou, B. Guo, P. X. Ma, *Biomaterials* **2016**, *104*, 18.
[4] E. J. Markvicka, M. D. Bartlett, X. Huang, C. Majidi, *Nat. Mater.* **2018**, *17*, 618.
[5] J. Xiong, G. Thangavel, J. Wang, X. Zhou, P. S. Lee, *Sci. Adv.* **2020**, *6*, eabb4246.
[6] Y. Cheng, K. H. Chan, X.-Q. Wang, T. Ding, T. Li, X. Lu, G. W. Ho, *ACS Nano* **2019**, *13*, 13176.
[7] L. Li, J. Meng, C. Hou, Q. Zhang, Y. Li, H. Yu, H. Wang, *ACS Appl. Mater. Interfaces* **2018**, *10*, 15122.
[8] W. Hu, G. Z. Lum, M. Mastrangeli, M. Sitti, *Nature* **2018**, *554*, 81.
[9] Y. Kim, H. Yuk, R. Zhao, S. A. Chester, X. Zhao, *Nature* **2018**, *558*, 274.
[10] J. Xiong, J. Chen, P. S. Lee, *Adv. Mater.* **2020**, *33*, 2002640.
[11] K. Li, Y. Shao, H. Yan, Z. Lu, K. J. Griffith, J. Yan, G. Wang, H. Fan, J. Lu, W. Huang, B. Bao, X. Liu, C. Hou, Q. Zhang, Y. Li, J. Yu, H. Wang, *Nat. Commun.* **2018**, *9*, 4798.
[12] Y. Kim, G. A. Parada, S. Liu, X. Zhao, *Sci. Rob.* **2019**, *4*, eaax7329.
[13] H.-W. Huang, M. S. Sakar, A. J. Petruska, S. Pané, B. J. Nelson, *Nat. Commun.* **2016**, *7*, 12263.
[14] J. Mu, G. Wang, H. Yan, H. Li, X. Wang, E. Gao, C. Hou, A. T. C. Pham, L. Wu, Q. Zhang, Y. Li, Z. Xu, Y. Guo, E. Reichmanis, H. Wang, M. Zhu, *Nat. Commun.* **2018**, *9*, 590.
[15] A. Miriyev, K. Stack, H. Lipson, *Nat. Commun.* **2017**, *8*, 596.
[16] Y. Yang, L. Shi, Z. Cao, R. Wang, J. Sun, *Adv. Funct. Mater.* **2019**, *29*, 1807882.
[17] J. Canadell, H. Goossens, B. Klumperman, *Macromolecules* **2011**, *44*, 2536.
[18] H. Ying, Y. Zhang, J. Cheng, *Nat. Commun.* **2014**, *5*, 3218.
[19] Y.-L. Liu, T.-W. Chuo, *Polym. Chem.* **2013**, *4*, 2194.
[20] Y. Chen, A. M. Kushner, G. A. Williams, Z. Guan, *Nat. Chem.* **2012**, *4*, 467.
[21] Y. Yanagisawa, Y. Nan, K. Okuro, T. Aida, *Science* **2018**, *359*, 72.
[22] J. Wu, L.-H. Cai, D. A. Weitz, *Adv. Mater.* **2017**, *29*, 1702616.
[23] N. Holten-Andersen, M. J. Harrington, H. Birkedal, B. P. Lee, P. B. Messersmith, K. Y. C. Lee, J. H. Waite, *Proc. Natl. Acad. Sci. USA* **2011**, *108*, 2651.
[24] M. Zhang, D. Xu, X. Yan, J. Chen, S. Dong, B. Zheng, F. Huang, *Angew. Chem., Int. Ed.* **2012**, *51*, 7011.
[25] D. C. Tuncaboylu, M. Sari, W. Oppermann, O. Okay, *Macromolecules* **2011**, *44*, 4997.
[26] S. Terryn, J. Brancart, D. Lefeber, G. Van Assche, B. Vanderborght, *Sci. Rob.* **2017**, *2*, eaan4268.
[27] H. Qin, T. Zhang, N. Li, H.-P. Cong, S.-H. Yu, *Nat. Commun.* **2019**, *10*, 2202.
[28] A. Pena-Francesch, H. Jung, M. C. Demirel, M. Sitti, *Nat. Mater.* **2020**, *19*, 1230.
[29] Q. Zhang, C.-Y. Shi, D.-H. Qu, Y.-T. Long, B. L. Feringa, H. Tian, *Sci. Adv.* **2018**, *4*, eaat8192.
[30] W. J. Chung, J. J. Griebel, E. T. Kim, H. Yoon, A. G. Simmonds, H. J. Ji, P. T. Dirlam, R. S. Glass, J. J. Wie, N. A. Nguyen, B. W. Guralnick, J. Park, Á. Somogyi, P. Theato, M. E. Mackay, Y.-E. Sung, K. Char, J. Pyun, *Nat. Chem.* **2013**, *5*, 518.
[31] P. Yan, W. Zhao, B. Zhang, L. Jiang, S. Petcher, J. A. Smith, D. J. Parker, A. I. Cooper, J. Lei, T. Hasell, *Angew. Chem., Int. Ed.* **2020**, *59*, 13371.
[32] Y. Xin, H. Peng, J. Xu, J. Zhang, *Adv. Funct. Mater.* **2019**, *29*, 1808989.
[33] Y. Deng, Q. Zhang, B. L. Feringa, H. Tian, D.-H. Qu, *Angew. Chem., Int. Ed.* **2020**, *59*, 5278.
[34] Z. R. Hinton, A. Shabbir, N. J. Alvarez, *Macromolecules* **2019**, *52*, 2231.
[35] E. B. Stukalin, L.-H. Cai, N. A. Kumar, L. Leibler, M. Rubinstein, *Macromolecules* **2013**, *46*, 7525.
[36] A. Campanella, D. Döhler, W. H. Binder, *Macromol. Rapid Commun.* **2018**, *39*, 1700739.
[37] I. Jeon, J. Cui, W. R. K. Illeperuma, J. Aizenberg, J. J. Vlassak, *Adv. Mater.* **2016**, *28*, 4678.
[38] M. A. Darabi, A. Khosrozadeh, R. Mbeleck, Y. Liu, Q. Chang, J. Jiang, J. Cai, Q. Wang, G. Luo, M. Xing, *Adv. Mater.* **2017**, *29*, 1700533.
[39] W. Huang, Y. Wang, Z. Huang, X. Wang, L. Chen, Y. Zhang, L. Zhang, *ACS Appl. Mater. Interfaces* **2018**, *10*, 41076.
[40] R. Tamate, K. Hashimoto, T. Horii, M. Hirasawa, X. Li, M. Shibayama, M. Watanabe, *Adv. Mater.* **2018**, *30*, 1802792.
[41] H. Guo, Y. Han, W. Zhao, J. Yang, L. Zhang, *Nat. Commun.* **2020**, *11*, 2037.
[42] T. Li, Y. Wang, S. Li, X. Liu, J. Sun, *Adv. Mater.* **2020**, *32*, 2002706.

© 2021 Wiley-VCH GmbH

[43] S.-M. Kim, H. Jeon, S.-H. Shin, S.-A. Park, J. Jegal, S. Y. Hwang, D. X. Oh, J. Park, *Adv. Mater.* **2018**, *30*, 1705145.
[44] J. A. Neal, D. Mozhdehi, Z. Guan, *J. Am. Chem. Soc.* **2015**, *137*, 4846.
[45] O. R. Cromwell, J. Chung, Z. Guan, *J. Am. Chem. Soc.* **2015**, *137*, 6492.
[46] Y. Cao, Y. J. Tan, S. Li, W. W. Lee, H. Guo, Y. Cai, C. Wang, B. C. K. Tee, *Nat. Electron.* **2019**, *2*, 75.
[47] J.-C. Lai, X.-Y. Jia, D.-P. Wang, Y.-B. Deng, P. Zheng, C.-H. Li, J.-L. Zuo, Z. Bao, *Nat. Commun.* **2019**, *10*, 1164.
[48] C.-H. Li, C. Wang, C. Keplinger, J.-L. Zuo, L. Jin, Y. Sun, P. Zheng, Y. Cao, F. Lissel, C. Linder, X.-Z. You, Z. Bao, *Nat. Chem.* **2016**, *8*, 618.
[49] J. Kang, D. Son, G.-J. N. Wang, Y. Liu, J. Lopez, Y. Kim, J. Y. Oh, T. Katsumata, J. Mun, Y. Lee, L. Jin, J. B. H. Tok, Z. Bao, *Adv. Mater.* **2018**, *30*, 1706846.
[50] X. Yan, Z. Liu, Q. Zhang, J. Lopez, H. Wang, H.-C. Wu, S. Niu, H. Yan, S. Wang, T. Lei, J. Li, D. Qi, P. Huang, J. Huang, Y. Zhang, Y. Wang, G. Li, J. B. H. Tok, X. Chen, Z. Bao, *J. Am. Chem. Soc.* **2018**, *140*, 5280.
[51] M. Liu, P. Liu, G. Lu, Z. Xu, X. Yao, *Angew. Chem., Int. Ed.* **2018**, *57*, 11242.
[52] S. J. Gerbode, J. R. Puzey, A. G. McCormick, L. Mahadevan, *Science* **2012**, *337*, 1087.
[53] Y. Cheng, R. Wang, K. H. Chan, X. Lu, J. Sun, G. W. Ho, *ACS Nano* **2018**, *12*, 3898.

© 2021 Wiley-VCH GmbH